Improving the Performance of Industrial Machines with Variable Stiffness Springs

Verstraten, Tom; Lopez Garcia, Pablo; Lenaerts, Bert; Mrak, Branimir; Lefeber, Dirk; Vanderborght, Bram

Published in:
Mechanics based design of structures and machines

DOI:
10.1080/15397734.2020.1713155

Publication date:
2022

License:
CC BY-NC

Document Version:
Accepted author manuscript

Improving the Performance of Industrial Machines with Variable Stiffness Springs

Tom Verstraten[a], Pablo Lopez-Garcia[a], Bert Lenaerts[b], Branimir Mrak[b], Dirk Lefeber[a], Bram Vanderborght[a]

[a] Robotics and Multibody Mechanics Research Group (R&MM), Vrije Universiteit Brussel and Flanders Make, 1050 Brussels, Belgium

[b]MotionS, Flanders Make, Leuven, Belgium

ABSTRACT

In several industrial applications, drivetrains impose highly dynamic oscillating motions to inertial loads. By introducing springs, the system's natural frequencies can be matched to the required operating frequencies, lowering energy consumption of the drivetrain. However, fixed-stiffness springs only have a positive effect in a limited range of frequencies. To solve this problem, variable stiffness springs are proposed. A discussion of the effect of the series and parallel topology, as well as the possibility of adapting the spatio-temporal characteristics of the motion to the spring, is presented. Furthermore, a practical implementation of a variable stiffness spring is proposed. Its effectiveness is validated in experiments.

KEYWORDS

Parallel Elastic Actuation; oscillating drivetrains; variable stiffness spring

1. Introduction

Many industrial processes require highly dynamic oscillating motions from relatively high masses. The high inertial loads result in peak power levels which are much higher than the average power requirement (Verstraten et al., 2015). As a result, the servo drivetrain needs to be composed of electric motors and power electronic components

Corresponding author. Email: Tom.Verstraten@vub.be

with high power ratings. In addition to the high investment cost of these components, the high peak powers and the oversized drivetrain will also result in high operational (energetic) costs. In other words, traditional servomotors are an inefficient, hence costly solution, even if they are selected optimally according to the well-established design principles such as inertia matching (Pasch and Seering, 1984) and other, more elaborate methods (Giberti et al., 2011; Richiedei, 2018).

The addition of energy buffers to oscillating drivetrains presents a potential solution to these problems. Electrical buffers (capacitors) only reduce the loading of the grid and the grid front end, mainly reducing the operational costs. Conversely, mechanical buffers (springs and flywheels) reduce the load on the motor and transmission, an effect which is also carried over further upstream to, again, the power electronics and grid. As a result, the drivetrain can be composed of smaller-sized, hence cheaper, components (Verstraten et al., 2018; Aló et al., 2018). Moreover, the reduced load on transmission components decreases energy losses in these components, an advantage which is exclusive to mechanical storage. In conclusion, mechanical buffers enable the strongest reduction in both operational and investment costs.

There is a large body of research on spring-assisted actuation in the field of robotics. Variable Stiffness Actuators (VSA) have a variable stiffness spring in between the drivetrain and the load. Such a series arrangement enables a reduction of the motor's speed requirements by, in the case of inertial loads, taking advantage of antiresonance (Verstraten et al., 2016). By varying the spring stiffness, the actuator can be tuned to any type of motion. There are several concepts of VSAs; an overview is given in Vanderborght et al. (2013). Each VSA type has its strengths and weaknesses, and must therefore be selected according to the application (Grioli et al., 2015).

Another possibility is to place the spring in parallel with the load. Here, the concept is that the parallel spring generates most of the nominal torque required to follow a given trajectory and the actuator only provides the difference (Verstraten et al., 2016). This way, the load on the motor is significantly reduced, so that less powerful and consequently lighter motors can be used. In industrial applications, parallel spring topologies – albeit with fixed stiffness – are much more prominent than series topologies. They

have been applied in, e.g., cryogenic coolers (Patt, 1985), piston compressors (Boldea et al., 1998) and four-bar linkage mechanisms (Lenaerts et al., 2018). Although most research in robotics is on series-topology VSAs, in recent years, several authors have investigated the use of parallel stiffness in actuation (Uemura and Kawamura, 2009; Iwamura et al., 2016; Nasiri et al., 2017). Other than in actuation, parallel springs are often used for gravity compensation of manipulators (Arakelian, 2016; Rosyid et al., 2019).

An issue with spring-assisted systems is the fact that a specific spring results in energy-optimal operation at a specific oscillation frequency (Verstraten et al., 2016). In some industrial applications, however, the operating frequency needs to be variable. Weaving looms, for example, operate in a specific frequency range in which the maximum frequency is typically the double of the minimum frequency (Adanur, 2000). In other words, depending on the operating condition, different stiffness values of the spring are optimal. The objective of this work is therefore to investigate the use of a spring with variable stiffness for oscillating motion in industrial applications. Specific questions which will be addressed are (i) What are the advantages and disadvantages of the series and parallel spring topology? (ii) How beneficial is variable stiffness, and how does it compare to the strategy of adapting the spatio-temporal trajectory? (iii) How can a variable stiffness spring be designed?

The document is structured as follows. In section 2, we will introduce the test case which will be used as a basis for this study. Next, in section 3, we will discuss two different strategies to deal with the need for varying frequencies: variable-stiffness spring assistance in a series and parallel spring topology and trajectory modulation. In section 4, we explain how variable parallel stiffness can be implemented in practice on a reciprocating machine, with special focus on the design of the variable stiffness spring itself and the required locking mechanisms. Experimental evidence for the successful implementation of the variable stiffness spring is presented in section 5. Finally, our conclusions are presented in section 6.

2. Test case: machine for reciprocating motion

The test case studied in this work is a low power oscillating drivetrain with motion and load conditions representative of an existing industrial machine. In this specific machine, the amount of power needed to move the load is small compared to the power needed to move the inertia of the drivetrain itself. In order to minimize the cost of the motors, it is important to keep the energy in the mechanical field. Frequent energy conversions between the mechanical and the electrical domain entail losses, which lead to higher peak power requirements in order to attain the required accelerations. Because of this, the size of the motor needs to increase and hence, the cost of the motor will increase which has a negative effect on the total cost of ownership (TCO).

2.1. *System model*

Due to its high oscillating frequencies, the load on the considered industrial machine is mainly inertial. The theoretical test case therefore consists of an inertial load of J_l = 4.1 gm^2. The machine is driven by a brushless DC motor, modeled as follows:

$$\begin{aligned} U &= k_t \dot{\theta}_m + RI \\ I &= \frac{1}{k_t} T_m \end{aligned} \tag{1}$$

with k_t the torque constant of the motor, R its winding resistance, U the voltage applied to the motor terminals and I the current drawn by the motor. $\dot{\theta}_m$ is the motor's output speed and T_m is the torque produced by the motor, which includes the inertial term $J_m \ddot{\theta}_m$ with rotor inertia J_m = 0.121 gm^2. Furthermore, in the theoretical evaluation, a transmission is considered with fixed gear ratio n. The value of n depends on the way the spring assistance is implemented (see section 3.1).

In order to prevent damage to the motor, following constraints are imposed to the motor:

$$\left| \dot{\theta}_m \right| < \dot{\theta}_{max} \tag{2}$$

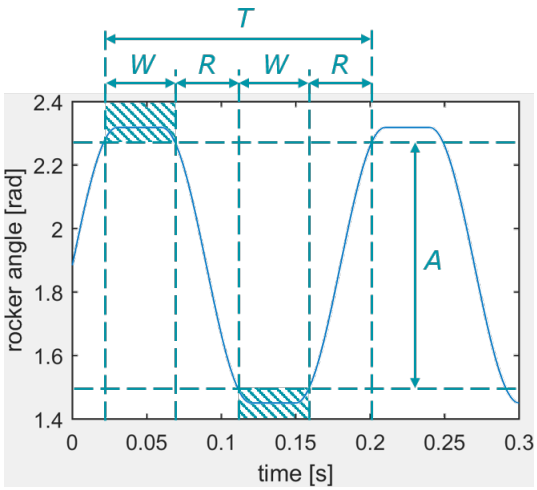

Figure 1. Output trajectory for the oscillating load.

$$[T_m]_{RMS} < T_{m,max,cont} \tag{3}$$

$$|T_m| < T_{m,max} \tag{4}$$

The values of the maximum motor speed $\dot{\theta}_{max} = 6000$ rpm, the maximum continuous motor torque $T_{m,max,cont} = 319$ mNm and the maximum motor torque $T_{m,max} = 1$ Nm correspond to the limits of the physical test setup presented in section 4.

2.2. *Imposed motion*

The main characteristic of the imposed motion is its frequency. The machine should be able to reach frequencies between 5 and 7 Hz. Furthermore, it should be possible to operate the mechanism in slow motion, at a speed of 1/3 Hz.

The exact trajectory of the motion is not predefined. It must, however, comply with several requirements. A visual representation of the imposed motion, along with its main parameters, is shown in Fig. 1. The load is held still at its extreme positions during a specified time period W. The minimal value for W is 30% of the total period T. The minimum distance between the two extreme positions, which is to be held during the time window W, is $A = 14°$. Note that the total range of the mechanism is

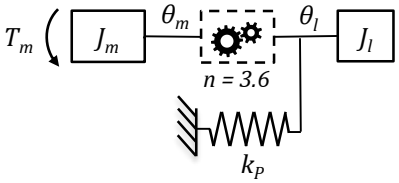

(a) Parallel Elastic Actuation (PEA)

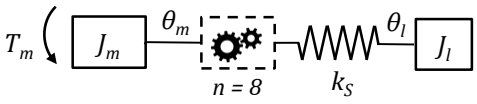

(b) Series Elastic Actuation (SEA)

Figure 2. Actuator topologies for spring assistance.

allowed to be higher than A.

3. Strategies for varying frequencies

3.1. *Spring assistance*

As explained in the introduction, the aim of this work is to evaluate the potential of spring-assisted solutions for oscillating drivetrains. By adding a spring to an inertial load, resonance and/or antiresonance frequencies are created, which can be exploited for energy-efficient operation (Beckerle et al., 2014). Two basic topologies exist for spring-assisted drivetrains: the series and parallel topology (Fig. 2). Comparative studies on both topologies on a pendulum setup showed that the series topology tends to be more efficient in exciting natural dynamics (Verstraten et al., 2016), as long as static loads are limited (Beckerle et al., 2017). This is the case for the application studied in this work. The aforementioned studies were, however, limited to purely sinusoidal motion, while the trajectory imposed in this case study exhibits a significant dwell period. As we will discuss in this section, this has considerable implications for the choice of spring topology.

Motor parameters (Maxon EC60 flat)	
Inertia J_m	0.121 gm^2
Nominal speed ω_{nom}	3490 rpm
Torque constant k_t	0.114 Nm/A
Winding resistance R	1.1 Ohm
Coulomb friction coefficient T_{Cm}	0.1089 Nm
Viscous friction coefficient ν_m	0.0024 Nm/(rad/s)
Gearbox parameters	
Gear ratio n	3.6 (PEA)
	8 (SEA)
Load parameters	
Inertia J_l	4.1 gm^2
Coulomb friction coefficient T_{Cl}	0.08 Nm
Viscous friction coefficient ν_l	0.01 Nm/(rad/s)

Table 1. List of parameters. If possible, parameter values were retrieved from datasheets. Friction coefficients were derived from experimental data. The inertia and friction coefficient values of the cam-follower mechanism were lumped together with those of the output to reduce the number of parameters.

3.1.1. Parallel Elastic Actuation

3.1.1.1. Equations. A drivetrain with a parallel spring is often referred to as a Parallel Elastic Actuator (PEA) (Verstraten et al., 2016). The equation of motion for the PEA on this setup is

$$\left(J_m + \frac{J_l}{n^2}\right)\ddot{\theta}_m + \left(T_{Cm} + \frac{T_{Cl}}{n}\right)\text{sign}\left(\dot{\theta}_m\right) + \left(\nu_m + \frac{\nu_l}{n^2}\right)\dot{\theta}_m + k_P\frac{\theta_m}{n^2} = T_m \qquad (5)$$

where n is the transmission ratio, J_m and J_l are the inertias of the motor and load, T_{Cm},T_{Cl} and ν_m,ν_l are the Coulomb and viscous friction coefficients on the motor (m) and load (l) side, k_P is the parallel spring stiffness, θ_m is the motor angle and T_m is the motor torque. A full list of parameters along with the values used in the simulations is given in Table 1. In our calculations, the transmission ratio is assumed to be constant. Note that, on the actual test setup described in section 4, a cam-follower mechanism and a linkage are installed, which make the transmission ratio n angle-dependent. Furthermore, the inertia of the parallel spring is assumed to be negligible with respect to the load inertia.

An explicit solution for the natural frequency can be found by neglecting friction

coefficients T_{Cm}, T_{Cl}, ν_m and ν_l in equation (5). We find

$$\theta_m = A_0 \cos(\omega t) \tag{6}$$

with

$$\omega = \sqrt{\frac{k_P}{J_m + \frac{J_l}{n^2}}} \tag{7}$$

To exploit the system's natural dynamics, we will therefore impose a stopped cosine as output motion, with an amplitude of $A_0 \geqq nA/2$ to meet the output amplitude requirement (see Section 2.2). Since the two dwell periods each represent a duration W of the total time period T of the motion, the period of the cosine will be $T - 2W$. In other words, the relationship between the machine's frequency f and the stopped cosine angular frequency ω is

$$\frac{1}{\omega} = \frac{1}{2\pi}\left(\frac{1}{f} - 2W\right) \tag{8}$$

The optimal stiffness setting thus becomes

$$k_{PEA,opt} = \left(J_m + \frac{J_l}{n^2}\right)\left(\frac{2\pi}{1/f - 2W}\right)^2 \tag{9}$$

Fig. 3 shows the torque that would be delivered by the motor with and without a parallel spring. While the torque during transitions from one stop to the other is significantly decreased by the parallel spring, it also leads to an additional torque being required during the dwell period to hold the tensioned spring. This torque would be more than the motor would be able to hold, as Joule losses heat up the windings from the motor. To make the parallel spring work, a mechanism would be required which locks the load as soon as the it reaches its extreme position, and unlocks it after the dwell time has passed. Such a locking mechanism would keep the load in place mechanically, so that the load is not transferred to the motor. However, it is challenging

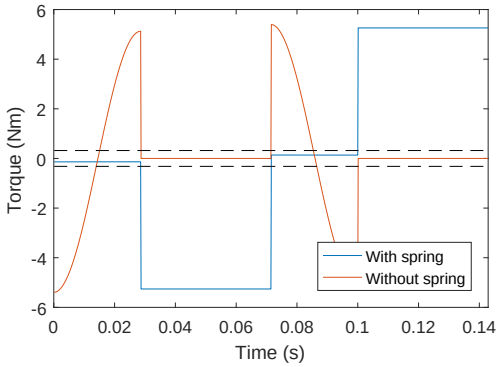

Figure 3. Torque seen by the motor in the setup with and without a parallel spring of 68 Nm/rad (the optimal value), for an imposed output motion of 7 Hz. The nominal torque of the motor is shown as a dashed line for reference.

to find a locking mechanism which is capable of a) reacting nearly immediately to a locking/unlocking command and b) locking and unlocking under load (Plooij et al., 2015). A practical, cam-based solution is proposed in section 4.1.3.

3.1.1.2. Electrical energy. Fig. 4 shows the electrical energy consumption of the drivetrain at various frequencies, for different stiffness settings. It is calculated by introducing equations (5) and (6) into (1), taking all relevant dissipative effects (friction as well as mechanical and electrical motor losses) into account. Only feasible solutions are shown in Fig. 4, i.e. the desired trajectory can be tracked without exceeding the motor limitations specified in section 2.1. Without parallel spring, only a range of 0-2.5 Hz can be achieved, much less than the goal of 7 Hz. When a parallel spring is added to the system, a resonance frequency is created where the torque is considerably lowered. A frequency of 7 Hz, for example, can easily be achieved with a spring of 68 Nm/rad. The optimal stiffness displays a quadratic dependence on the resonance frequency (red line), in line with the approximated equation (7) where friction was neglected. Any frequency near the resonance frequency (in a band of ca. 1-1.5 Hz) can be achieved by the actuator.

Recall that the ability to perform slow motion (oscillation at a frequency of 0.3 Hz) was one of the requirements. As seen in Fig. 4, this is only possible for parallel spring stiffness values up to 9 Nm/rad. At higher stiffness values, the spring will counteract the imposed motion rather than support it, resulting in an increased torque required

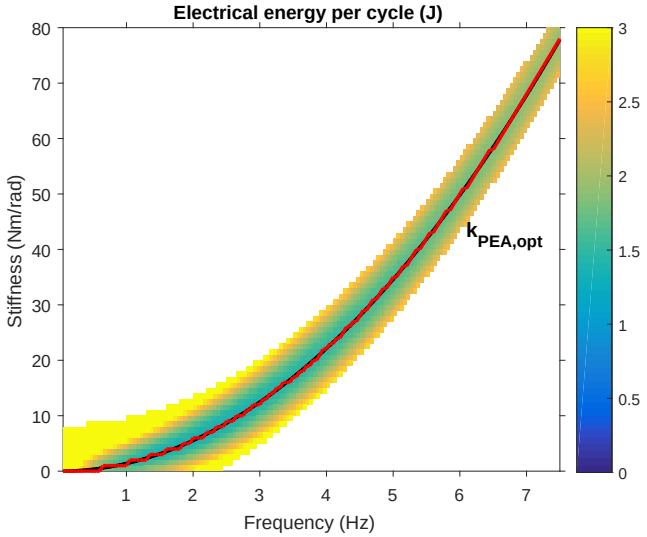

Figure 4. Electrical energy consumption of the PEA setup as a function of oscillation frequency and spring stiffness. The energy-optimal spring stiffness (red dotted line) coincides perfectly with the theoretically optimal spring stiffness $k_{PEA,opt}$ (black) calculated by means of (9).

from the motor. For this reason, many PEAs are equipped with clutches (Plooij et al., 2017). If the stiffness of the parallel spring is variable, one could of course bring its stiffness down to zero. For many variable stiffness concepts, however, extremely low stiffness settings are hard to realize in practice. This is the case for the VSA concept implemented in this work (see Section 4).

3.1.2. Series Elastic Actuation

From the discussion above, two important disadvantages of the PEA emerged. The first is the need for a mechanism to lock the load during the dwell period, the second is the difficulty to perform slow motion. In this regard, a topology where the spring is placed in series with the drivetrain rather than in parallel presents an interesting alternative. This topology, which is typically referred to as a Series Elastic Actuator (SEA) (Verstraten et al., 2016), is discussed below.

3.1.2.1. Equations. The equation of motion for the SEA is given by following system of differential equations

$$J_m\ddot{\theta}_m + T_{Cm}\text{sign}\left(\dot{\theta}_m\right) + \nu_m\dot{\theta}_m + \frac{k_S}{n}\left(\frac{\theta_m}{n} - \theta_l\right) = T_m \tag{10}$$

$$J_l\ddot{\theta}_l + T_{Cl}\text{sign}\left(\dot{\theta}_l\right) + \nu_l\dot{\theta}_l - k_S\left(\frac{\theta_m}{n} - \theta_l\right) = 0 \tag{11}$$

where k_S represents the stiffness of the series spring and θ_l the load angle (see Fig. 2). Again, the gear ratio n is assumed to be constant, and the inertia of the spring negligible.

The next step is to find the natural frequency. By neglecting friction, equations (10) and (11) can be simplified to a single biquadratic equation

$$\frac{nJ_mJ_l}{k_S}\theta_l^{(4)} + \left(nJ_m + \frac{J_l}{n}\right)\ddot{\theta}_l = T_m \tag{12}$$

Besides the trivial solution $\omega = 0$, the solution to this differential equation with $T_m = 0$ is a cosine with frequency

$$\omega_{SEA,r} = \sqrt{\frac{k_S\left(J_m + J_l/n^2\right)}{J_mJ_l}} \tag{13}$$

This is the resonance frequency of the system. The corresponding series spring stiffness is

$$k_{SEA,r} = \frac{J_mJ_l}{J_m + J_l/n^2}\left(\frac{2\pi}{1/f - 2W}\right)^2 \tag{14}$$

The series elastic element of an SEA can also be exploited to decrease motor speed, which is given by

$$\dot{\theta}_m = n\left(\dot{\theta}_l + \frac{J_l\dddot{\theta}_l}{k_S}\right) \tag{15}$$

A piecewise solution which minimizes motor speed can thus be found by solving the differential equation (15) with $\dot{\theta}_m$=0. Neglecting friction ($T_{Cl} = 0$, $\nu_l = 0$), the solution would once again be a cosine. The only difference is the different expression for the

frequency:

$$\omega_{SEA,a} = \sqrt{\frac{k_S}{J_l}} \tag{16}$$

This is the antiresonance frequency of the system. The series spring stiffness corresponding to this frequency is

$$k_{SEA,a} = J_l \left(\frac{2\pi}{1/f - 2W} \right)^2 \tag{17}$$

Note that, unlike the resonance frequency, the antiresonance frequency is independent of the drivetrain inertia. This is because, at antiresonance, rotation of the drivetrain is minimized. Hence, its inertia no longer contributes to the torque to be delivered, and the only load on the motor is the inertial load caused by the acceleration of the load. Consequently, the SEA benefits not only from a reduction in motor speed, but also from a moderate reduction in motor torque. In Verstraten et al. (2016), the authors showed that, for this reason, antiresonance tends to be a more energy-efficient operating frequency than resonance if the load is mainly inertial. Of course, because motor torque is only partially decreased in an SEA whereas, in theory, it is completely reduced to zero in a PEA, the SEA will require a larger gear reduction than the PEA.

Also note that, in contrast to the parallel spring of the PEA, the series spring of an SEA does not provide a position-dependent torque to the load. As a result, the motor of an SEA will not need to deliver any torque during the dwell phase, nor will it have to deliver excessive torques to enable slow motion at (inappropriately) high spring stiffness values.

3.1.2.2. Electrical energy. The electrical energy consumption of the SEA-driven machine , which is calculated by introducing equations (12) and (15) into (1), is shown in Fig. 5. Again, all relevant dissipative effects (i.e. friction as well as motor losses) are taken into account. The figure clearly shows the SEA's inherent ability to generate slow motion: at any stiffness in the range of the graph, frequencies from 0-3 Hz can

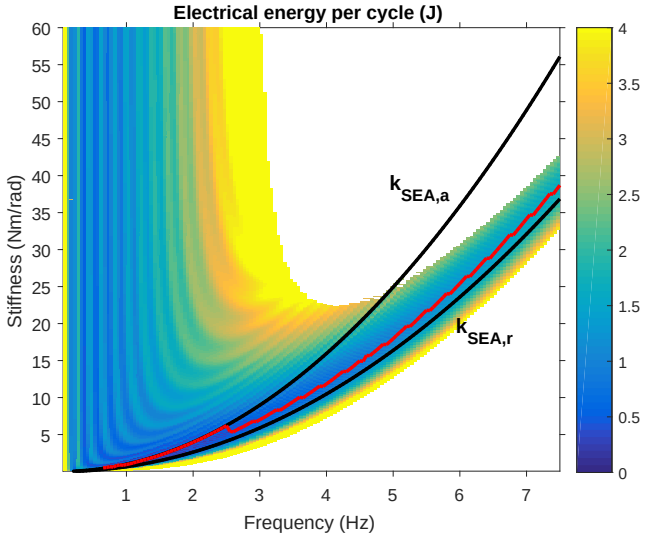

Figure 5. Energy consumption of the SEA setup. The minimal energy consumption for any frequency is denoted by the red dashed line. Antiresonance and resonance frequencies are denoted by black lines.

be attained at all but the very lowest stiffness settings. Note that, in comparison with the PEA setup, the same motor is used, but the gear ratio has been increased from $n = 3.6$ to $n = 8$.

Interestingly, minimal energy consumption corresponds to antiresonance only at the lowest frequencies. For frequencies above approximately 3 Hz, it occurs at a stiffness setting closer to resonance. This seemingly contrasts with the results obtained on a SEA-driven pendulum in Verstraten et al. (2016), where it was shown that antiresonance is the preferred operating point across the entire frequency range, but supports those in Beckerle et al. (2017), where the same shift was observed on a similar setup. The differences are explained by the limitations of the motor. Fig. 5 shows that antiresonance can no longer be attained frequencies above 5 Hz because the motor's torque limit is exceeded. The ideal operating point at high frequencies therefore inevitably moves to resonance, where the motor torque is decreased. This is also what happened in Beckerle et al. (2017), although the authors did not specifically investigate motor limitations in this work. In Verstraten et al. (2016), however, the motor of the SEA was oversized, allowing it to work within the studied frequency range when the series spring was replaced by a rigid connection. Consequently, the motor did not exceed its torque limits during the SEA experiments, and the optimal working point remained at

antiresonance. To summarize, these results demonstrate that the sizing of the motor – more specifically its torque limit – has a decisive impact on the selection of working points for the SEA.

3.1.3. Conclusion

From the discussion above, it emerges that the optimal stiffness of the SEA setup for a specific operating frequency is harder to determine for the SEA than for the PEA. Another major issue with the SEA is the fact that its output motion is more difficult to control due to non-collocation with the output (Eppinger and Seering, 1989). Strong transients during start-up or close to the outer stops may be the consequence. The stopped cosine which was suggested as output trajectory, for example, has a discontinuous second derivative. This causes Dirac pulses to appear in the third derivative of the output position θ_l, which is a part of the expression for the motor speed (15). Consequently, tracking the trajectory will require a Dirac pulse in motor speed as well. Physically speaking, this translates to the requirement of instantaneous motion between two positions, which is of course impossible to meet. It is therefore necessary to smoothen the desired output trajectory.

In conclusion, while the SEA has several advantages in terms of mechanical design, it comes at the cost of a complicated control design. For this reason, in the following, the SEA topology will be abandoned, and we will focus on the PEA instead.

3.2. *Trajectory Modulation*

In some cases it is possible to change the imposed motion in such a way that the main natural frequency matches the stiffness setting. This is also a valid option on the studied test setup. As explained in Section 3.1.1.1, the optimal spring stiffness is defined by the imposed frequency of the oscillation, but also by the length of the dwell period (Eq. (9)). Recall from section 2.2 that only a minimum length of 30% of the total period was set out for the dwell period. By increasing the length W of the dwell period, the range of frequencies which can be attained with a specific spring stiffness can be increased to lower frequencies. This is illustrated in Fig. 6. The minimum frequency

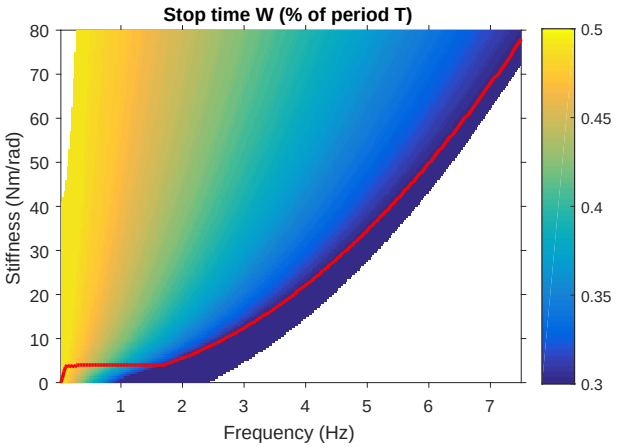

Figure 6. Attainable frequencies of the PEA setup, for various stiffness settings and frequencies. The energy-optimal length of the dwell time is indicated by the color map. The red line indicates the energy-optimal stiffness and dwell time for every frequency.

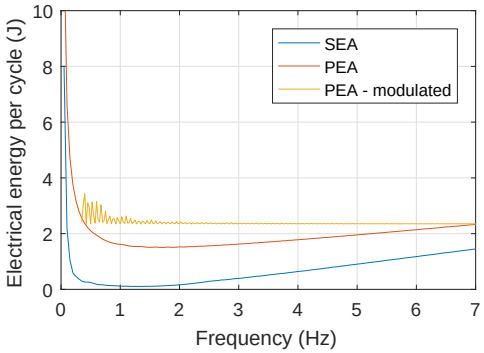

Figure 7. Electrical energy consumption of the variable-stiffness SEA (blue), the variable-stiffness PEA (red) and a fixed-stiffness PEA (parallel stiffness of 70 Nm/rad) with trajectory modulation (orange).

requirement, 1/3 Hz for slow-motion, is met for stiffness values up to 80 Nm/rad, the optimal stiffness for operation at 7.5 Hz. In other words, trajectory modulation would enable to use of a PEA with fixed stiffness. In conclusion, like variable stiffness, trajectory modulation increases the range of attainable frequencies.

3.3. *Energetic comparison*

To conclude, the strategies discussed in this section are compared in terms of electrical energy consumption. Figure 7 shows the electrical energy consumption per cycle of the variable-stiffness SEA and PEA topology, as well as that of a fixed-stiffness PEA with trajectory modulation. For the variable-stiffness SEA and PEA, the optimal stiffness is selected for each frequency. For the fixed-stiffness PEA, a spring stiffness of $k_P = 70$

Nm/rad is selected, as it enables oscillation frequencies up to 7 Hz – the requirement set out in section 2.2. The length of the dwell time is adjusted to the frequency as explained in section 3.2.

From Figure 7, we can conclude that the SEA is the best solution in terms of energy-efficiency. This is in line with the results from Verstraten et al. (2016), where the SEA was found to generate oscillations more efficiently than a PEA on a pendulum setup. Furthermore, the variable-stiffness PEA is found to be more efficient than the fixed-stiffness PEA with trajectory modulation. We can thus conclude that, although trajectory modulation enlarges the range of attainable frequencies, it does not offer the same benefits as variable stiffness in terms of reduction of energy consumption.

4. Implementation

In order to validate the findings from the previous section, a variable stiffness spring was implemented on a test setup representative of an existing industrial machine. For the reasons explained in section 3.1.3, a parallel spring was preferred over a series spring. The design of the setup and the variable stiffness parallel spring are explained below.

4.1. *Test setup*

The test setup is depicted in Fig. 8. Its purpose is to generate the reciprocating motion required in a real-life industrial process, while replicating the required torques on a smaller scale. In an earlier work, the drivetrain of the machine was assisted by a torsion spring with fixed stiffness in parallel with the drivetrain (Mrak et al., 2015). The considered industrial process, however, requires a specific frequency range in which the maximum frequency is typically the double of the minimum frequency. In this work, the fixed-stiffness spring is therefore replaced by a spring with variable stiffness which accommodates the entire range of operating frequencies.

The selection and design of the most crucial components are explained below.

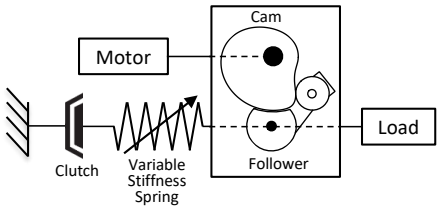

(a) Schematic of the test setup.

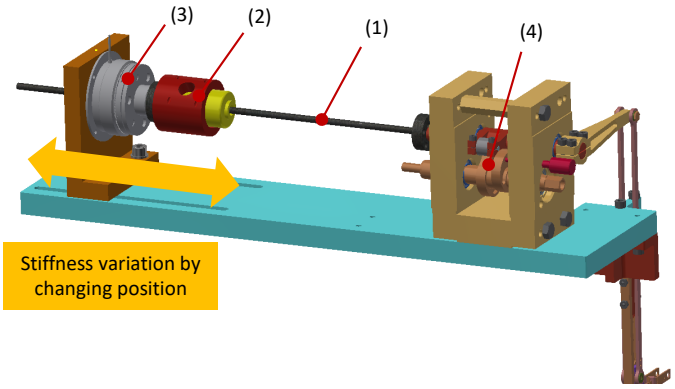

(b) CAD drawing of the test setup.

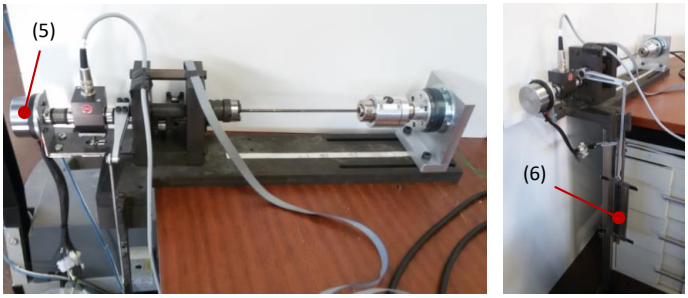

(c) Physical test setup.

Figure 8. Test setup with variable parallel stiffness. Major components: (1) Torsion bar, (2) 3-jaw chuck, (3) Electromagnetic clutch for slow motion, (4) Cam-follower mechanism, (5) DC motor, (6) Load mass.

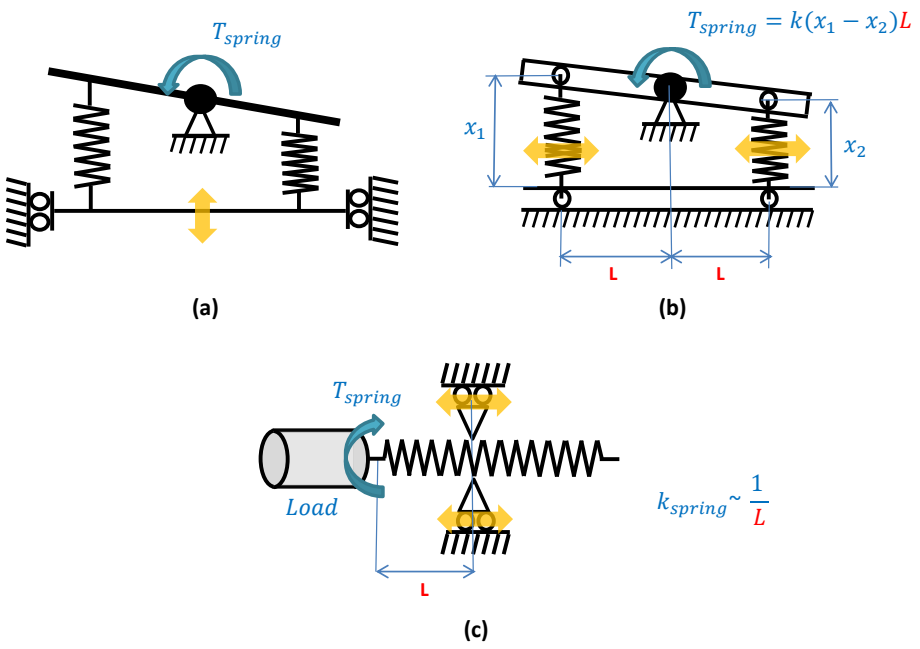

Figure 9. Proposed solutions for variable parallel springs, based on Vanderborght et al. (2013): (a) Spring preload adjustment, (b) Changing transmission between load and spring, (c) Changing physical properties of spring. The spring stiffness adjustment is denoted by an orange arrow.

4.1.1. Variable stiffness concepts

For the design of the variable stiffness spring, we took inspiration from the large body of work on Variable Stiffness Actuators (VSAs). Note that VSAs are essentially actuators with a spring placed in series between the motor and load. This is in contrast with the test setup in this work, where the spring is placed in parallel to the load.

In an extensive review paper by Vanderborght et al. (2013), three different categories of adaptable stiffness are proposed. A schematic of these solutions, applied to the considered setup, is depicted in Fig. 9.

4.1.1.1. Spring preload adjustment. A first method to create variable stiffness behavior is to change the preload of the springs. The review paper by Vanderborght et al. (2013) divides this concept into three subconcepts: preload adjustment of a single spring, antagonistic springs with antagonistic motors, and antagonistic springs with independent motors. The last class is depicted in Fig. 9a. A major disadvantage of these systems is that the force required to change stiffness increases monotonically with the desired stiffness. Another disadvantage is the fact that input energy is needed

to hold a certain stiffness setting (Chalvet and Braun, 2017), unless if non-backdrivable mechanisms (worm gears, brakes or other locking mechanisms) are added to the design.

4.1.1.2. Changing transmission between load and spring. Unlike concepts based on spring preload adjustment, concepts which change the transmission ratio between the load and the spring can be made intrinsically energy-efficient, since the force required to change the stiffness at equilibrium is perpendicular to the spring displacement. As explained in Vanderborght et al. (2013), there are several ways to change the transmission ratio: by changing lever length, by introducing a nonlinear mechanical link, or by using a continuously variable transmission (CVT). Practical implementations of this type of actuator based on a planetary differential can be found in Kim and Song (2012); Cui et al. (2014).

4.1.1.3. Changing physical properties of spring. The physical properties of an elastic element can essentially be changed in three ways: by changing its material properties, its geometry, or its length. Stiffness variation based on the length of the elastic element – or equivalently, in the case of helical springs, on the number of coils – is probably the simplest and most versatile out of these three options. It has been implemented on designs with helical springs (Hollander et al., 2005), torsion rods (Schuy et al., 2013) and, most commonly, leaf springs (Morita and Sugano, 1995; Choi et al., 2011; Braun et al., 2016; Fang and Wang, 2018). Note that all examples listed here, except for Braun et al. (2016), employ a series spring and not a parallel spring as in this work.

4.1.2. Design of a variable length torsion rod

On the test setup, we opted for a torsion rod with variable length. A potential issue with controlling stiffness through the length of the elastic element is play. The ideal clamping element must be able to move axially, while providing zero play in the radial direction. These requirements are particularly hard to meet if continuous variation throughout the motion is required.

On the test setup, only a single stiffness setting is required at a time, as the industrial process occurs at a fixed frequency - which may, however, be varied between runs. This

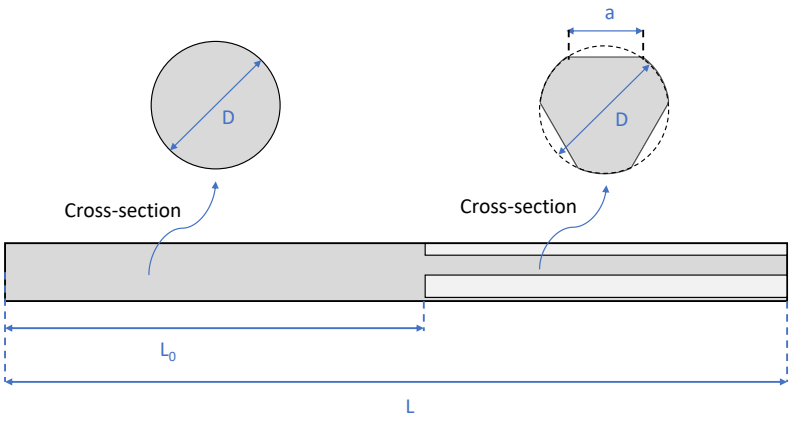

Figure 10. Design of the torsion rod for the variable stiffness spring.

allows the usage of a three-jaw chuck as a clamping element. The three-jaw chuck enables secure, free of play clamping, but must be tightened or loosened when the torsional element is not moving. In other words, stiffness variation must be carried out at machine standstill and can thus not be done continuously, but the issue of play is completely eliminated.

The design of the torsion rod relies on the basic formulas for torsion of a beam. The optimal cross-section in terms of lifetime is circular. However, to enable better clamping of the three-jaw chuck, three flats, each $a = 1.5\text{mm}$ wide, are milled onto the round bar over a length $L - L_0$ used for stiffness variation (see Fig. 10). The polar moment of inertia for this type of shaft (diameter D) is given by

$$J_v = \left(1 - 3 \cdot \operatorname{atan2}\left(\frac{\sqrt{D^2 - a^2}}{D}, \frac{a}{D}\right)\right) \frac{\pi D^4}{32} + \frac{3}{32}\left(\frac{a^3}{3D^3} + \frac{a}{D}\right)\left(D^2 - a^2\right)^2 \tag{18}$$

The torque supplied by the parallel spring as a function of the deflection is

$$T_{spring}\left(L\right) = k\left(L\right)\Delta\theta \tag{19}$$

with spring stiffness k given by

$$k\left(L\right) = G\left(\frac{L_0}{J_0} + \frac{L - L_0}{J_v}\right)^{-1} \tag{20}$$

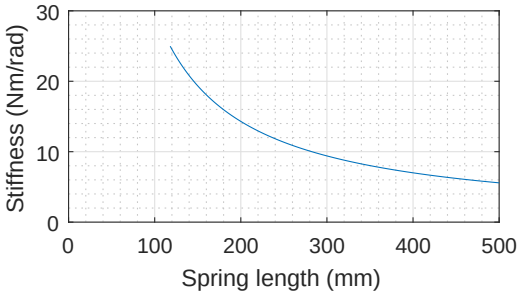

Figure 11. Stiffness vs. length of a Cr-Si steel alloy torsion rod with a diameter of $D = 4.4$ mm and a round-section length of $L_0 = 120$ mm. Only stiffness values which respect the strength calculation are plotted.

with G the material's shear modulus, $J_0 = \pi D^4/32$ the polar moment of inertia of a circular rod, L_0 the partial length of the rod with full circular cross-section, and L the total length of the rod, which is varied in the proposed design.

The maximum achievable stiffness is limited by the maximum allowable stress in the rod, τ_{max}. Following the standard equations for torsion on a beam, and after some simple manipulations, the maximum shear stress can be expressed with the formula

$$\tau_{max}(L) = \frac{G J_0 \Delta\theta_{max} R}{J_v L_0 + J_0 (L - L_0)} \tag{21}$$

with $R = D/2$ the radius of the rod and $\Delta\theta_{max}$ the maximum deflection, in this case 16°. Using this formula, we implicitly assume that the highest stress occurs in the circular part of the rod (largest distance to center). A Cr-Si spring steel alloy ($G = 80$ GPa, $\tau_{max} = 1.32$ GPa) was used as construction material because of its superior strength and durability.

Employing a safety factor of 3, we can construct force-length diagrams for different diameters. Fig. 11 shows such a diagram for the torsion rod used in the test setup. The length of the actual torsion rod was limited to a maximum of L=300 mm for reasons of space and a minimum of 120 mm (corresponding to the length L_0) for reasons of strength. The resulting stiffness variation range is 9-25 Nm/rad.

4.1.3. Locking mechanism

The simulations revealed that the PEA requires a locking mechanism in order to limit the energy consumption during the dwell periods of the motion. To generate a dou-

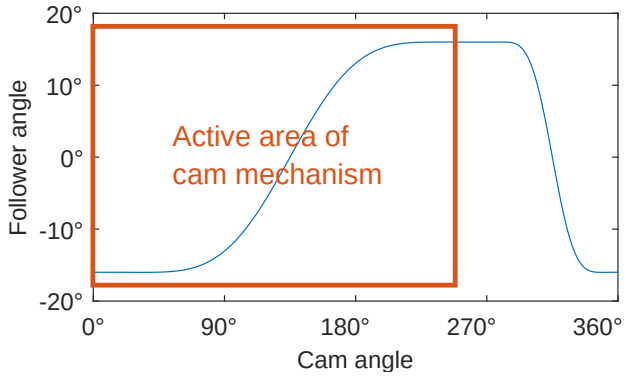

Figure 12. Cam mechanism kinematics.

ble dwell period, the setup is equipped with a cam-follower mechanism. Cam-follower mechanisms have been utilized for ages in different types of machinery to create this type of dwell motion (Adanur, 2000). They have also been implemented in PEA designs for active prostheses with the aim of shaping the linear torque-angle characteristic of the parallel spring to a more desirable nonlinear characteristic (Realmuto et al., 2015; Gao et al., 2018). Compared to a discrete locking mechanism such as e.g. a controllable clutch, the cam-follower mechanism has the distinct advantage that it smoothens out the acceleration profile. Moreover, it is completely passive. The downside is that their strongly nonlinear characteristic presents some serious additional challenges in terms of control.

The angular kinematics of the cam-follower mechanism on the test setup is visualized in Fig. 12. The cam input angle is intended to be between (approximately) 0 and 270 °. At the outer ends of this range, which correspond to follower angles of approximately 16 °, the follower angle is unaffected by the cam angle, i.e., it is locked. The mechanism can rest in this position, while no torque has to be delivered by the motor. To put the equilibrium angle of the parallel spring exactly in between these two extremes, a calibration pin can be inserted into alignment holes in the cam profile and in the fixed structure.

4.1.4. Clutch for slow motion

A well-known issue with parallel springs is that, when they are tuned to compensate for the inertial torque at high-frequency oscillations, they counteract the motion at low speeds. This causes excessive motor torques at low frequencies and problems at the start of the motion, which can potentially be solved by "swinging up" the load to the desired amplitude or by starting the setup from its highest amplitude – something which can be achieved thanks to the cam mechanism. However, these solutions still do not enable slow motion of the device. To solve this problem, the setup was equipped with a clutch. When the clutch is disengaged, the parallel spring is decoupled from the load, so that it will no longer deliver a torque to the device which would have to be counteracted by the motor at low speeds. Following the selection procedure suggested by Plooij et al. (2015), an electromagnetically actuated dog clutch was selected.

4.1.5. Motor and gearbox

The motor used on the test setup is the same Maxon EC60 flat motor as the one used in the simulations (specifications listed in Table 1). No gearbox is added to the motor, as the cam-follower mechanism already provides an average gear ratio of approximately 3.6, in line with the value used for the PEA simulations.

4.2. *Control*

Iterative learning control (ILC) gradually adapts the input signal $u(t) = T_m$ to create more accurate tracking at the output, without making any changes to the controller itself. ILC is highly robust to systematic disturbances or system uncertainties, but its performance can be degraded by noise or nonrepeating disturbances. Taking these characteristics into consideration, the repetitive nature of the motion and of potential disturbances make ILC the logical option for control of the test setup.

Out of the many possible options for ILC, we selected the inverted plant method (Bristow et al., 2006) using a second-order linearized system model as a basis. The

control input $u(\lambda)$ at discrete time λ of iteration $j+1$ is calculated from

$$u_{j+1}(\lambda) = u_j(\lambda) + \hat{P}^{-1}(q)e_j(\lambda) \tag{22}$$

where q is the forward-time operator defined by

$$qx\,(\lambda) = x\,(\lambda + 1) \tag{23}$$

The error e is the difference between the imposed motor position θ_m, which is determined from the desired output profile by means of inverse dynamic calculations, and the measured motor position $\hat{\theta}_m$:

$$e(\lambda) = \theta_m(\lambda) - \hat{\theta}_m(\lambda) \tag{24}$$

The matrix P can be determined from the plant's state-space representation:

$$\begin{aligned} x_j\,(\lambda + 1) &= Ax_j(\lambda) + Bu_j(\lambda) \\ y_j(\lambda) &= Cx_j(\lambda) \end{aligned} \tag{25}$$

With these equations, the matrix P becomes

$$P = C\,(qI - A)^{-1}\,B \tag{26}$$

The plant model was obtained from identification, by fitting the second-order transfer function onto experimental data using Matlab's System Identification toolbox. The experimental data was obtained by applying a chirp signal to the input, with a stiffness setting in the middle of the available range. Although the coefficients in the ILC algorithm depend on the selected stiffness setting, the influence of the stiffness term appeared to be relatively small, and the coefficients obtained with an intermediate stiffness setting led to a decent performance at other stiffness settings as well.

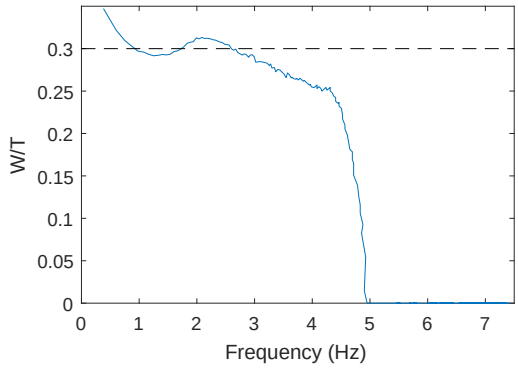

Figure 13. Swept sine experiment without spring assistance (i.e. $k_P = 0$ Nm/rad). The ratio minimum requirement of 30% for the ratio W/T, as defined in section 2.2, is respected for most frequencies up to 2.6 Hz.

4.3. *Sensors and data acquisition*

The (linear) position of the load mass is derived from the measurement of the motor position θ_m, utilizing the known kinematic relationships of the cam-follower mechanism (Fig. 12) and the linkage. The motor position θ_m is measured by a CUI Devices AMT10 encoder and acquired by a Maxon EPOS3 drive. The EPOS3 drive takes care of the low-level (current) control of the Maxon EC60 flat motor and transfers the motor position signal to the high-level (ILC) controller, which generates the current setpoint for the EPOS3. The high-level controller, running at 1kHz, is implemented in Matlab Simulink on a commercial laptop, utilizing the Beckhoff TwinCAT environment to achieve EtherCAT-based real-time communication between the real-time host and the EPOS3 drive. The details of this implementation are described in (Langlois et al., 2018).

5. Experiments

5.1. *Without spring assistance*

In order to evaluate the need for spring assistance, we first conducted a baseline experiment to determine which frequency range can be attained by the drivetrain itself. For this experiment, a simple linearized feedback controller (Slotine et al., 1991) was designed to control the position of the motor. Knowing that a sinusoidal motor trajectory with an amplitude of at least 100° generates the desired output trajectory, a

swept sine of this amplitude was used as desired trajectory. The frequency was varied between 0.33 and 7 Hz. With this input signal, the imposed motor speed does not exceed 1833 rpm, which is well below the nominal speed of the motor (3490 rpm, see Table 1). In other words, the only factor which can limit the attainable frequencies is the maximum motor current (or torque).

Results are shown in Fig. 13. The minimum threshold of W/T = 0.3 (see the motion requirements in section 2.2) is maintained for frequencies up to 2.6 Hz, except for a small range of frequencies between 0.9 - 1.7 Hz which, due to tuning of the controller and friction effects, narrowly misses the threshold value. Above 2.6 Hz, the motor current starts to saturate, and the drivetrain effectively becomes undersized for this range of frequencies. This result is in accordance with the theoretical results presented in section 3.1.1, where a zero-stiffness frequency range of 0 - 2.5 Hz was predicted.

5.2. *With spring assistance*

The next step is to evaluate whether assistance from a parallel spring can effectively increase the frequency range that can be reached by the actuator. To do so, we conducted a series of experiments, imposing various constant frequencies at three distinct stiffness settings (k_P = 10.1,10.8 and 14.9 Nm/rad). The ILC controller described in section 4.3 was used to impose the prescribed motion to the output. The results are shown in Fig. 14. Frequencies at which the output motion complied with the requirement $W/T > 0.3$, as defined in section 2.2, are marked in green, while unsuccessful trials are marked in red. The trend of increasing stiffness for increasing frequencies, as predicted in the simulations, is clearly visible in this measurement (dashed line). One may, however, notice that the experimentally observed resonance frequency is higher than the one obtained from the simulations in section 3.1.1, presented in Fig. 4. Possible reasons for this deviation from the simulations are (i) the nonlinear kinematics of the cam-follower mechanism, which were linearized in the simulations, (ii) due to actuator saturation, the ILC-controlled drivetrain may yield a different output trajectory which, nevertheless, still complies with the requirements, (iii) friction parameters of the setup may have been altered by the introduction of the variable stiffness mechanism, (iv)

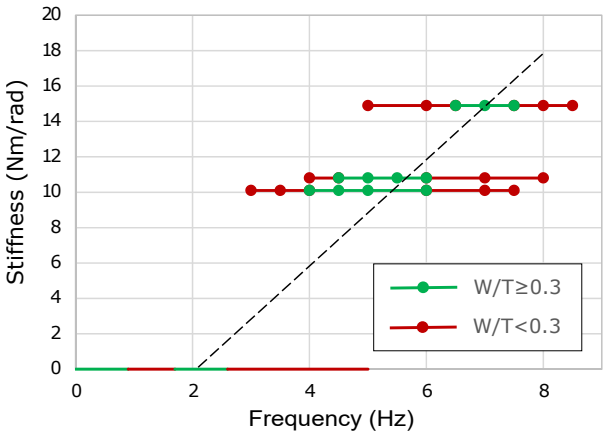

Figure 14. Measurement with parallel spring. Markers denote measurements at discrete combinations of frequencies and stiffness values. Green markers indicate that the requirement $W/T > 0.3$ is met; red markers indicate that it is not. The measurements at zero stiffness are taken from the swept sine experiment from section 5.1. There is a clear trend towards increasing stiffness for increasing frequency (dashed line).

the cam-follower mechanism exhibits unmodeled compliance. The additional inertia of the spring was ruled out as a potential reason for deviations, as it is four orders of magnitude smaller than the inertia of the load mass.

Most importantly, Fig. 14 shows that motion at frequencies between 5 and 7 Hz, as well as slow motion at 1/3 Hz, are possible. Hence, the requirements set out in section 2.2 are met. We can therefore conclude that the implementation of the proposed variable stiffness spring on the test setup has been successful.

6. Conclusion

In this paper, we studied the potential of variable-stiffness spring assistance for oscillating drivetrains. An industrial low-power reciprocating machine was used as a test case to evaluate the benefits of series springs, parallel springs and trajectory modulation in terms of motor size and energy consumption. We presented a practical design for a variable-stiffness parallel spring, which was implemented in a test rig representative of the industrial machine and its load conditions. In experiments and simulations, we showed that this variable-stiffness parallel spring, combined with a well-designed locking mechanism, extends the frequency range that can be achieved with a specific drivetrain. In other words, variable stiffness springs enable smaller motors to be used,

which is beneficial in terms of investment cost. Moreover, by avoiding high power peaks, power losses can be brought down, which is beneficial in terms of operational costs. In conclusion, variable stiffness springs present a huge potential for a reduction in total cost of ownership (TCO).

Acknowledgments

The first author is a postdoctoral fellow of the Research Foundation - Flanders (FWO). This work was funded by the IWT-ICON project PROFENSTO (grant no. 150530), by the European Research Council starting grant SPEAR (grant no. 337596) and by Flanders Make vzw.

References

Adanur, S. (2000). *Handbook of Weaving*. CRC Press.

Aló, R., F. Bottiglione, and G. Mantriota (2018). Flywheel-infinitely variable transmissions for energy recovery capabilities in artificial knee joints. *Mechanics Based Design of Structures and Machines 46*(3), 333–346.

Arakelian, V. (2016). Gravity compensation in robotics. *Advanced Robotics 30*(2), 79–96.

Beckerle, P., F. Stuhlenmiller, and S. Rinderknecht (2017). Stiffness control of variable serial elastic actuators: Energy efficiency through exploitation of natural dynamics. *Actuators 6*(4).

Beckerle, P., T. Verstraten, G. Mathijssen, R. Furnémont, B. Vanderborght, and D. Lefeber (2017, Feb). Series and parallel elastic actuation: Influence of operating positions on design and control. *IEEE/ASME Transactions on Mechatronics 22*(1), 521–529.

Beckerle, P., J. Wojtusch, S. Rinderknecht, and O. von Stryk (2014). Analysis of system dynamic influences in robotic actuators with variable stiffness. *Smart Structures and Systems 13*(4), 711–730.

Boldea, I., C. Wang, B. Yang, and S. A. Nasar (1998, Oct). Analysis and design of

flux-reversal linear permanent magnet oscillating machine. In *Conference Record of 1998 IEEE Industry Applications Conference. Thirty-Third IAS Annual Meeting (Cat. No.98CH36242)*, Volume 1, pp. 136–143 vol.1.

Braun, D. J., S. Apte, O. Adiyatov, A. Dahiya, and N. Hogan (2016, May). Compliant actuation for energy efficient impedance modulation. In *2016 IEEE International Conference on Robotics and Automation (ICRA)*, pp. 636–641.

Bristow, D. A., M. Tharayil, and A. G. Alleyne (2006, June). A survey of iterative learning control. *IEEE Control Systems 26*(3), 96–114.

Chalvet, V. and D. J. Braun (2017, Aug). Criterion for the design of low-power variable stiffness mechanisms. *IEEE Transactions on Robotics 33*(4), 1002–1010.

Choi, J., S. Hong, W. Lee, S. Kang, and M. Kim (2011, April). A robot joint with variable stiffness using leaf springs. *IEEE Transactions on Robotics 27*(2), 229–238.

Cui, Z., H. Yang, D. Qian, Y. Cui, and Y. Peng (2014, Dec). Development of a novel variable stiffness actuator with automatic rigidity/compliance switching. In *2014 IEEE International Conference on Robotics and Biomimetics (ROBIO 2014)*, pp. 326–331.

Eppinger, S. D. and W. P. Seering (1989, May). Three dynamic problems in robot force control. In *Robotics and Automation, 1989. Proceedings., 1989 IEEE International Conference on*, pp. 392–397 vol.1.

Fang, L. and Y. Wang (2018). Study on the stiffness property of a variable stiffness joint using a leaf spring. *Proceedings of the Institution of Mechanical Engineers, Part C: Journal of Mechanical Engineering Science 0*(0), 0954406218761221.

Gao, F., Y. Liu, and W.-H. Liao (2018, March). Design of powered ankle-foot prosthesis with nonlinear parallel spring mechanism. *Journal of Mechanical Design 140*(5), 055001–055001–8.

Giberti, H., S. Cinquemani, and G. Legnani (2011). A practical approach to the selection of the motor-reducer unit in electric drive systems. *Mechanics Based Design of Structures and Machines 39*(3), 303–319.

Grioli, G., S. Wolf, M. Garabini, M. Catalano, E. Burdet, D. Caldwell, R. Carloni, W. Friedl, M. Grebenstein, M. Laffranchi, D. Lefeber, S. Stramigioli, N. Tsagarakis,

M. Van Damme, B. Vanderborght, A. Albu-Schaeffer, and A. Bicchi (2015). Variable stiffness actuators: The user's point of view. *The International Journal of Robotics Research 34*(6), 727–743.

Hollander, K. W., T. G. Sugar, and D. E. Herring (2005, June). Adjustable robotic tendon using a 'Jack Spring' ™. In *9th International Conference on Rehabilitation Robotics, 2005. ICORR 2005.*, pp. 113–118.

Iwamura, M., S. Imafuku, T. Kawamoto, and W. Schiehlen (2016). *Design and Control of an Energy-Saving Robot Using Storage Elements and Reaction Wheels*, pp. 277–297. Cham: Springer International Publishing.

Kim, B. S. and J. B. Song (2012, Oct). Design and control of a variable stiffness actuator based on adjustable moment arm. *IEEE Transactions on Robotics 28*(5), 1145–1151.

Langlois, K., T. van der Hoeven, D. Rodriguez Cianca, T. Verstraten, T. Bacek, B. Convens, C. Rodriguez-Guerrero, V. Grosu, D. Lefeber, and B. Vanderborght (2018, March). Ethercat tutorial: An introduction for real-time hardware communication on windows [tutorial]. *IEEE Robotics Automation Magazine 25*(1), 22–122.

Lenaerts, B., A. Abdallh, D. Maes, B. Mrak, T. Galle, and W. De Waele (2018, August). Total cost of ownership optimization of manufacturing machines with fast energy storage. In *18th International Conference on Power Electronics and Motion Control.*

Morita, T. and S. Sugano (1995, May). Design and development of a new robot joint using a mechanical impedance adjuster. In *Robotics and Automation, 1995. Proceedings., 1995 IEEE International Conference on*, Volume 3, pp. 2469–2475 vol.3.

Mrak, B., W. Driesen, and W. Desmet (2015). Magnetic springs: Fast energy storage for reciprocating industrial drivetrains. In *Proceedings of 23rd ABCM International Congress of Mechanical Engineering.*

Nasiri, R., M. Khoramshahi, M. Shushtari, and M. N. Ahmadabadi (2017, April). Adaptation in variable parallel compliance: Towards energy efficiency in cyclic tasks. *IEEE/ASME Transactions on Mechatronics 22*(2), 1059–1070.

Pasch, K. A. and W. Seering (1984). On the drive systems for high-performance machines. *Journal of Mechanical Design 106*(1), 102–108.

Patt, P. (1985, Sep). Design and testing of a coaxial linear magnetic spring with integral linear motor. *IEEE Transactions on Magnetics 21*(5), 1759–1761.

Plooij, M., G. Mathijssen, P. Cherelle, D. Lefeber, and B. Vanderborght (2015, March). Lock your robot: A review of locking devices in robotics. *IEEE Robotics Automation Magazine 22*(1), 106–117.

Plooij, M., W. Wolfslag, and M. Wisse (2017, April). Clutched elastic actuators. *IEEE/ASME Transactions on Mechatronics 22*(2), 739–750.

Realmuto, J., G. Klute, and S. Devasia (2015, March). Nonlinear passive cam-based springs for powered ankle prostheses. *Journal of Medical Devices 9*(1), 011007–011007–10.

Richiedei, D. (2018). Integrated selection of gearbox, gear ratio, and motor through scaling rules. *Mechanics Based Design of Structures and Machines 0*(0), 1–18.

Rosyid, A., B. El-Khasawneh, and A. Alazzam (2019). Gravity compensation of parallel kinematics mechanism with revolute joints using torsional springs. *Mechanics Based Design of Structures and Machines 0*(0), 1–21.

Schuy, J., P. Beckerle, J. Faber, J. Wojtusch, S. Rinderknecht, and O. Von Stryk (2013, July). Dimensioning and evaluation of the elastic element in a variable torsion stiffness actuator. In *Advanced Intelligent Mechatronics (AIM), 2013 IEEE/ASME International Conference on*, pp. 1786–1791.

Slotine, J.-J. E., W. Li, et al. (1991). *Applied nonlinear control*, Volume 199. Prentice-Hall Englewood Cliffs, NJ.

Uemura, M. and S. Kawamura (2009, May). Resonance-based motion control method for multi-joint robot through combining stiffness adaptation and iterative learning control. In *Robotics and Automation, 2009. ICRA '09. IEEE International Conference on*, pp. 1543–1548.

Vanderborght, B., A. Albu-Schaeffer, A. Bicchi, E. Burdet, D. Caldwell, R. Carloni, M. Catalano, O. Eiberger, W. Friedl, G. Ganesh, M. Garabini, M. Grebenstein, G. Grioli, S. Haddadin, H. Hoppner, A. Jafari, M. Laffranchi, D. Lefeber, F. Petit, S. Stramigioli, N. Tsagarakis, M. Van Damme, R. Van Ham, L. Visser, and S. Wolf (2013). Variable impedance actuators: A review. *Robotics and Autonomous*

Systems 61(12), 1601 – 1614.

Verstraten, T., P. Beckerle, R. Furnémont, G. Mathijssen, B. Vanderborght, and D. Lefeber (2016). Series and parallel elastic actuation: Impact of natural dynamics on power and energy consumption. *Mechanism and Machine Theory 102*, 232–246.

Verstraten, T., L. Flynn, J. Geeroms, B. Vanderborght, and D. Lefeber (2018). On the electrical energy consumption of active ankle prostheses with series and parallel elastic elements. In *2018 7th IEEE International Conference on Biomedical Robotics and Biomechatronics (BioRob)*, pp. 720–725.

Verstraten, T., G. Mathijssen, R. Furnémont, B. Vanderborght, and D. Lefeber (2015). Modeling and design of geared DC motors for energy efficiency: Comparison between theory and experiments. *Mechatronics 30*, 198 – 213.